PHYSICAL REVIEW B **105**, 174438 (2022)

Spin-phonon and magnetoelectric coupling in oxygen-isotope substituted $TbMnO_3$ investigated by Raman scattering

P. J. Graham,[1] P. Rovillain,[1,2,3] M. Bartkowiak,[4,5] E. Pomjakushina,[6] K. Conder,[6]
M. Kenzelmann,[7] and C. Ulrich[1,*]
[1]*School of Physics, The University of New South Wales, Sydney, New South Wales 2052, Australia*
[2]*The Australian Centre for Neutron Scattering, Australian Nuclear Science and Technology Organisation, Lucas Heights, New South Wales 2234, Australia*
[3]*Sorbonne Université, CNRS, Institut des NanoSciences de Paris, INSP, UMR7588, F-75005 Paris, France*
[4]*School of Physical, Environmental and Mathematical Sciences, University of New South Wales, Canberra, Australian Capital Territory 2600, Australia*
[5]*Helmholtz-Zentrum Berlin für Materialien und Energie, Hahn-Meitner Platz 1, D-14109 Berlin, Germany*
[6]*Laboratory for Multiscale Materials Experiments, Paul Scherrer Institute, CH-5232 Villigen, Switzerland*
[7]*Laboratory for Neutron Scattering and Imaging, Paul Scherrer Institute, CH-5232 Villigen, Switzerland*

(Received 13 September 2021; revised 16 January 2022; accepted 15 February 2022; published 31 May 2022)

In order to investigate the effects leading to the strong magnetoelectric coupling in the type II multiferroic $TbMnO_3$ we have studied the thermal properties and temperature dependence of the lattice vibrations of $TbMn^{16}O_3$ and its isotopically substituted counterpart $TbMn^{18}O_3$. Heat capacity measurements on powder samples revealed no significant change in the Mn^{3+} and Tb^{3+} magnetic phase transition temperatures, as well as the multiferroic ordering temperature upon isotope substitution, indicating that a change in the dynamical modulation of the MnO_6 octahedral distortions and rotations altering the Mn-O-Mn bond angles has no influence on the magnetic properties of $TbMnO_3$. Raman light scattering experiments have been performed on isotopically substituted single crystals to determine the temperature induced changes in phonon energies and linewidths at the sinusoidal and multiferroic phase transitions. A detailed modeling indicates that the spin-phonon coupling can be accounted for the pronounced anomalies in the temperature dependence of the phonon behaviors at the transition to the sinusoidal spin phase at $T_N^{Mn} = 41$ K and to the multiferroic spin-spiral phase at $T_{FE} = 28$ K. No further effects such as the appearance of the electric polarization or the electromagnon were required to explain the data, especially below the multiferroic phase transition.

DOI: 10.1103/PhysRevB.105.174438

I. INTRODUCTION

Multiferroic materials have drawn tremendous interest due to their potential for the development of new and innovative applications in solid-state technologies [1–4]. They exhibit coexisting ferroelectricity and magnetic order and in the case of type II multiferroics both properties can even be switched by each other [1,5,6]. This makes them extremely useful, for example, in spintronics [7], novel sensor applications [8], or as memory devices in IT technology where the data storage capacity could be increased by five to six orders of magnitude [9]. Terbium manganite ($TbMnO_3$) is such a multiferroic material which demonstrates a strong magnetoelectric (ME) coupling and has therefore been the subject of intensive research in particular on the investigation of the mechanisms behind its ME coupling [5]. However, due to the complex spin, charge, and orbital interactions in these systems, the underlying quantum-mechanical processes responsible for these phenomena are still not fully understood.

Essentially, two approaches provide explanations for the microscopic mechanism for the ME coupling in $TbMnO_3$. The semiempirical Dzyaloshinskii-Moriya interaction (DMI) model of Sergienko and Dagotto considers the interplay between the DMI and the elastic energy of the crystal for a noncollinear spin ordering [10]. This leads to a relative displacement between the Mn^{3+} and O^{2-} ions and hence induces an electric polarization. In the model of Katsura, Nagaosa, and Balatsky, a spin-current induced by a spin-spiral generates an electric polarization, which is proportional to $\mathbf{P} \propto \mathbf{r}_{i,j} \times (\mathbf{S}_i \times \mathbf{S}_j)$ [11], where $\mathbf{r}_{i,j}$ is the propagation direction of the magnetic spiral (i.e., along the *b* axis in $TbMnO_3$), and $\mathbf{S}_i \times \mathbf{S}_j$ describes the spin rotation axis, which is perpendicular to the spin rotation plane, the *bc* plane in the case of $TbMnO_3$. The resulting electric polarization in $TbMnO_3$ is therefore along the *c* axis as observed in experiments [5,6]. However, the model does not specify whether the mechanism is a purely electronic phenomenon caused by charge displacements, or if it involves atomic displacements [4]. To achieve the value of the experimentally determined electric polarization, the expected atomic displacements would be in the range of 0.001 Å, which is at the limits of current diffraction techniques. Walker *et al.* used circularly polarized synchrotron x-ray diffraction with an applied magnetic field and determined that the displacement of the Tb^{3+} ions of −21(3) fm caused by exchange striction is the origin of

---

[*] Corresponding author: c.ulrich@unsw.edu.au

the electric polarization [12,13]. By simultaneously analyzing high resolution x-ray synchrotron and powder neutron diffraction data of oxygen-isotope substituted $\mathrm{DyMn^{18}O_3}$ and $\mathrm{DyMn^{16}O_3}$ we have determined that the atomic displacements are in the order of 0.5×10^{-12} m, i.e., in the subpicometer range [14]. However, the precise mechanism of the ME coupling in $\mathrm{TbMnO_3}$ still remains unsolved.

$\mathrm{TbMnO_3}$ crystallizes in the orthorhombically distorted perovskite crystal structure with the space group *Pbnm*, D_{2h}^{16} (No. 62 in the "International Tables for Crystallography" [15]) and the corresponding lattice parameters are $a = 5.3$ Å, $b = 5.86$ Å, and $c = 7.49$ Å at 300 K [16]. This structure can be regarded as a three-dimensional network of corner-sharing $\mathrm{MnO_6}$ octahedra. The $\mathrm{GeFeO_3}$-type distortion leads to $\mathrm{MnO_6}$ octahedral rotations that are antiferrodistortive (out of phase) around $[100]_c$ and $[010]_c$, and ferrodistortive (in phase) around $[001]_c$ ($a^-a^-b^+$ in Glazer notation) in the pseudocubic notation of the unit cell. Upon cooling, $\mathrm{TbMnO_3}$ undergoes three magnetic phase transitions: $T_\mathrm{N}^\mathrm{Mn} = 41$ K, $T_\mathrm{FE} = 28$ K, and $T_\mathrm{N}^\mathrm{Tb} = 7$ K [16–18]. At 41 K, the $\mathrm{Mn^{3+}}$ spins order in an incommensurate sinusoidal magnetic structure with a propagation vector along the *b* direction and $(0, k \pm \tau_y, 1)$ where τ_y is ~0.29. At $T_\mathrm{FE} = 28$ K, $\mathrm{TbMnO_3}$ undergoes a combined magnetic and ferroelectric phase transition. An electric polarization appears along the *c* axis that is relatively weak ($P_c \approx 8 \times 10^{-4}\ \mathrm{C\,m^{-2}}$ at 10 K) as compared to typical proper ferroelectrics [19]. However, the interest in $\mathrm{TbMnO_3}$ comes from its strong ME coupling between the electric and magnetic degrees of freedom [19]. At the ferroelectric phase transition, the $\mathrm{Mn^{3+}}$ spins reorient from a sinusoidal to a spin-spiral structure with a magnetic propagation vector along the *b* axis and the spins being arranged within the *bc* plane. The length of the propagation vector decreases systematically from $\tau_y \approx 0.288$ at $T_\mathrm{N}^\mathrm{Mn} = 41$ K to $\tau_y \approx 0.2765$ near 32 K, and then remaining almost constant down to lowest temperatures with small changes at the ferroelectric/spin-spiral phase transition at 28 K and upon the sinusoidal ordering of the $\mathrm{Tb^{3+}}$ moments at 7 K [16–18]. This indicates that the spin structure remains incommensurate and no lock-in transition occurs in the entire temperature range. The resonant magnetic x-ray scattering experiments by Prokhnenko *et al.* showed that an induced ordering of $\mathrm{Tb^{3+}}$ moments sets in already at about $T_\mathrm{FE} = 28$ K with a modulation identical to the $\mathrm{Mn^{3+}}$ spin-spiral order, i.e., $\tau_1^\mathrm{Tb} = \tau^\mathrm{Mn} \approx 0.28$ [20]. A similar behavior was observed for $\mathrm{DyMnO_3}$ [14]. Furthermore, the magnetoelastic coupling induces a lattice modulation with $\tau_l = 0.56 = 2\tau_y$ below the ferroelectric phase transition [5,21]. This displacement is symmetric and therefore does not contribute to the electric polarization. Finally, below $T_\mathrm{N}^\mathrm{Tb} = 7$ K, the ordering of the $\mathrm{Tb^{3+}}$ moments occurs with $\tau_2^\mathrm{Tb} = 0.426$.

The incommensurate magnetic structure of $\mathrm{TbMnO_3}$ is the result of competing short-range nearest-neighbor (NN) and long-range next-nearest-neighbor (NNN) magnetic interactions. Along the *c* direction, the antiferromagnetic (AFM) exchange interaction $J_c > 0$ is a combination of both anisotropic e_g^1-O($2p$)-e_g^1 and isotropic t_{2g}^3-O($2p$)-t_{2g}^3 interactions. In the *ab* plane, the NN interaction is composed of a strong anisotropic ferromagnetic (FM) e_g^1-O($2p$)-e_g^1 and a weaker isotropic AFM t_{2g}^3-O($2p$)-t_{2g}^3 interaction, overall giving a FM $J_{ab} < 0$. In addition, an AFM next-nearest-neighbor interaction in the *b* direction $J_b > 0$ exists via a Mn-O-O-Mn exchange path [5,22,23]. Furthermore, exchange interactions between the $\mathrm{Tb^{3+}}$ and $\mathrm{Mn^{3+}}$ ions ($J_\text{Mn-Tb}$) may also require careful consideration [20]. Overall, the competition between NN and NNN interactions in the *ab* plane results in a highly frustrated magnetic spin system in $\mathrm{TbMnO_3}$ and is the reason for the sinusoidal and spiral-spin structures.

In order to further elucidate the mechanism that leads to the magnetoelectric coupling in multiferroic $\mathrm{TbMnO_3}$, we have performed Raman light scattering and specific heat measurements on $\mathrm{TbMn^{16}O_3}$ and its isotopically substituted counterpart $\mathrm{TbMn^{18}O_3}$. Changing the oxygen mass affects the lattice vibrations directly and therefore alters the magnetic exchange interactions through the modulation of the Mn-O-Mn bond angles and octahedral distortions. In our previous high resolution x-ray synchrotron and neutron diffraction experiment we have determined the precise crystallographic and magnetic structure of $\mathrm{DyMn^{16}O_3}$ and its isotopically substituted counterpart $\mathrm{DyMn^{18}O_3}$ [14]. The data show distinct differences in the crystal structure between both isotopically substituted $\mathrm{DyMnO_3}$ samples. For example, the Mn-O2(a) bond length inside the $\mathrm{MnO_6}$ octahedra increases and the bond length Mn-O2(b) decreases for the $\mathrm{O^{18}}$ substituted sample, while the bond length Mn-O1 remains almost constant.

To determine the isotope effect on the different magnetic phase transitions in $\mathrm{TbMnO_3}$, precise heat capacity measurements were performed. It has previously been demonstrated that isotope substitution can result in dramatic changes of the electronic and magnetic properties of transition metal oxides. For example, in the 1950s isotope substitution did provide key evidence for a phonon-mediated coupling mechanism of the Cooper pairs in superconductors, supporting the development of the BCS theory [24,25]. However, for high-temperature superconductors such as $\mathrm{YBa_2Cu_3O_7}$, the substitution of $\mathrm{O^{16}}$ with the heavier $\mathrm{O^{18}}$ resulted in a significantly smaller shift of the superconducting phase transition as expected for the Fröhlich interaction, which indicated that lattice vibrations are not the main contribution to the coupling mechanism of Cooper pairs [26–30]. In $\mathrm{(La_{0.25}Pr_{0.75})_{0.7}Ca_{0.3}MnO_3}$ the temperature of the metal-insulator transition drops almost linearly from 95 K for pure $\mathrm{O^{16}}$ to 50 K for 39% $\mathrm{O^{18}}$ content, where the material becomes metallic [31]. A further example is quantum paraelectric $\mathrm{SrTiO_3}$ where the decrease of the soft phonon mode with oxygen isotope substitution results in a phase transition to a ferroelectric state at finite temperature [32–34]. Isotope substitution therefore provides an important avenue to explore the role of lattice dynamics on the physical properties of a material, that is otherwise inaccessible with other techniques. This is of particular importance for $R\mathrm{MnO_3}$ multiferroics, where according to the DMI model the electric polarization originates from a relative displacement between the $\mathrm{Mn^{3+}}$ and $\mathrm{O^{2-}}$ ions.

Raman light scattering experiments were performed to reveal the temperature dependence of the phonon modes upon entering the magnetic and multiferroic phases. The observed pronounced changes in the temperature dependence of the phonon energies and linewidths can serve as an indication for subtle changes in structural, magnetic, and ferroelectric degrees of freedom, i.e., they can be caused by spin-phonon coupling [35,36] or by interactions with the

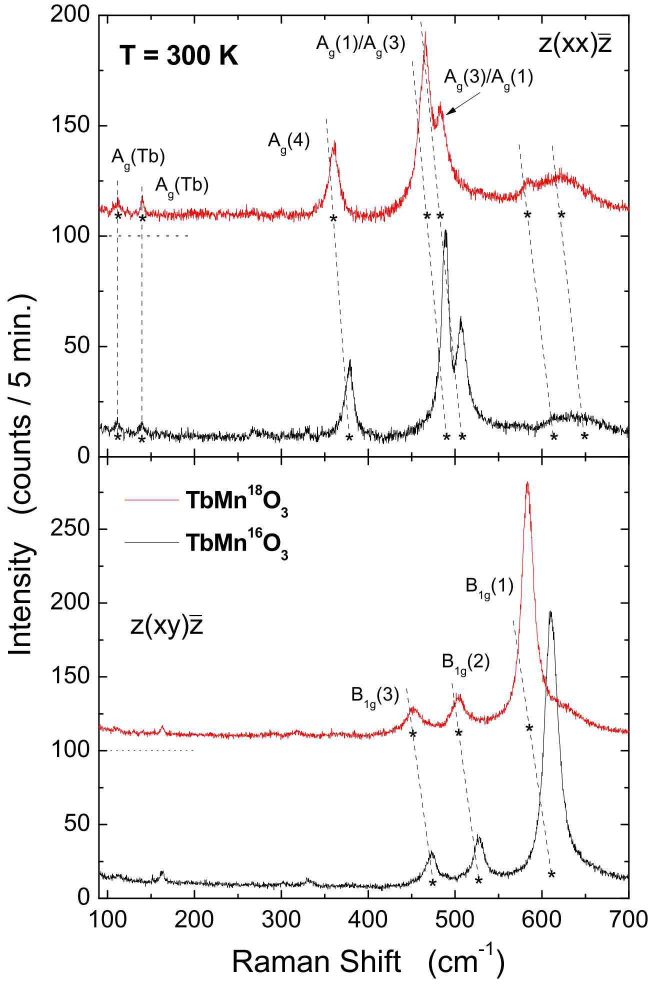

FIG. 1. A comparison of the Raman spectra of O^{16} and O^{18}-substituted $TbMnO_3$ single crystals taken at 300 K. The upper panel shows the data taken in $z(xx)\bar{z}$ and the lower panel the data taken in $z(xy)\bar{z}$ polarization. The dashed lines indicate the assignment of the observed phonon modes according to Iliev *et al.* [42,43]. In the O^{18}-substituted sample the phonon modes which involve the movement of oxygen ions, appear at ~5% lower energy as compared to $TbMn^{16}O_3$. From this shift in phonon frequency the concentration of the oxygen-isotope O^{18} was determined to be $97.7 \pm 1.0\%$ in $TbMn^{18}O_3$.

electric polarization (i.e., polarons [37–39]). Therefore, Raman light scattering experiments offer further insights into the mechanism responsible for the magnetoelectric coupling in multiferroics such as $TbMnO_3$.

II. EXPERIMENTAL DETAILS

A large high-quality $TbMnO_3$ single crystal was grown using the traveling solvent floating-zone technique. The sample was then divided into two daughter crystals. Both were subsequently annealed at elevated temperatures under identical condition, with one sample being annealed in O^{18}-isotope atmosphere and the other in pure oxygen in its natural abundance of 99.762% O^{16}. As such, this sample can be regarded as $TbMn^{16}O_3$. Raman scattering data taken at a temperature of 300 K are shown in Fig. 1. Changing the mass of the oxygen changes the frequency of a phonon mode in first approximation by $\sqrt{k/M}$, where k is the force constant which is related to the interatomic potential and M is the reduced mass of the corresponding vibration. Here k can be assumed to be constant [40]. From the observed oxygen-isotope induced phonon shifts we were able to determine the O^{18} oxygen content for the O^{18}-treated crystal sample to be $97.7 \pm 1.0\%$ in the surface region. A cut through the $TbMn^{18}O_3$ single crystal did indicate that during annealing the O^{18} atoms had a finite penetration depth into the crystal. However, this did not affect the results of the Raman light scattering experiment due to the finite penetration depth of light of about 200 nm with the used laser wavelength of 568 nm [41]. But it did necessitate the growth of isotopically substituted powder samples for the specific heat measurements, where the increase in surface-to-volume ratio overcomes this problem of oxygen-isotope substitution. A parent sample of $TbMnO_3$ powder was synthesized via standard solid-state reaction methods and divided into two samples, which were then annealed at identical temperatures in O^{18}-isotope atmosphere and in natural oxygen. Raman scattering measurements of the phonon energies of both samples determined an estimated O^{18} oxygen content for the $TbMn^{18}O_3$ powder sample of $68 \pm 3\%$, in reasonable agreement with a content of $60 \pm 10\%$ determined via mass thermogravimetry. Specific heat measurements were then performed using a physical property measurement system (PPMS) of the company Quantum Design.

Raman spectra were acquired with a Dilor XY triple-monochromator spectrometer in backscattering geometry using the 568 nm laser line of an Ar^+/Kr^+ mixed gas laser for excitation. This particular line was chosen because of the resonance enhanced phonon intensities, the reduced photoluminescence background, and the high spectral resolution at this line. To avoid laser induced heating of the sample, the power of the incident laser beam was set to 5 mW with a laser spot size of $\approx 100\ \mu$m diameter at the sample position. The temperature dependence of the Raman spectrum was determined in the range from 13 to 300 K using a Leybold Heraeus cryostat equipped with a helium capillary. The scattering geometry was chosen to be $z(xx)\bar{z}$ and $z(xy)\bar{z}$ in the Porto notation, which allows for the observation of the A_g and B_{1g} modes, respectively. The modes were then analyzed by fitting Voigt profiles to the measured spectra. The Voigt line shape corresponds to the convolution of a Lorentzian shaped phonon line with the Gaussian shape instrumental resolution, which was determined independently to be 2.8 cm^{-1} by taking calibration scans for each Raman spectrum using the spectral lines of a neon light source. The calibration scans served also to determine the precise energy positions of the phonons.

III. RESULTS AND DISCUSSION

A. Heat capacity measurements of the isotope substituted samples

Figure 2 shows the temperature dependence of the heat capacity for both the O^{16} and the 68% isotopically substituted O^{18} $TbMnO_3$ powder samples in the low-temperature range. The specific heat at the phase transitions is λ shaped, which indicates that the transitions are of second order. The precise

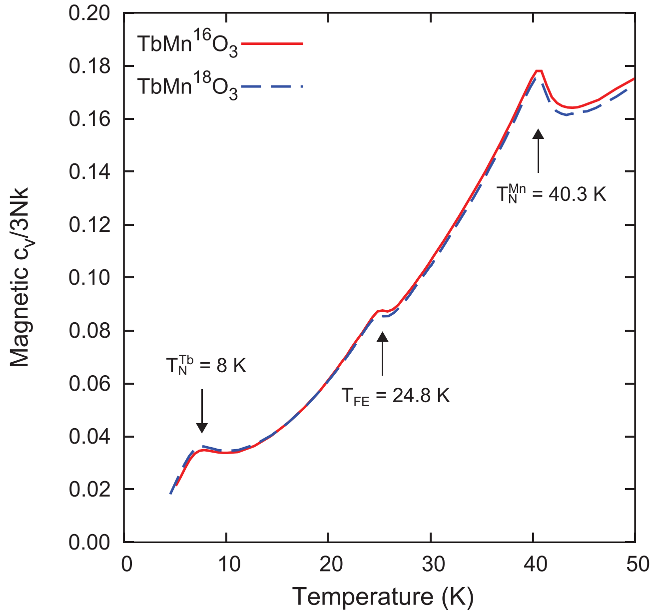

FIG. 2. Heat capacity measurements of the TbMn^{16}O$_3$ and the 68% oxygen-isotope substituted TbMn^{18}O$_3$ powder samples. The phase transition temperatures were determined by fitting λ-shaped curves, which is characteristic for a second-order phase transition, to the experimental data. The determined magnetic phase transition temperatures do not show any significant changes upon oxygen-isotope substitution.

temperature of the magnetic phase transitions was determined by fitting the formula for the critical exponent to the data. The magnetic phase transitions appear at $T_N^{Mn} = 40.3(1)$ K [40.1(1) K] to the sinusoidal AFM order, at $T_{FE} = 24.8(1)$ K [24.8(1) K] to the ferroelectric and Mn^{3+} spin-spiral order, and at $T_N^{Tb} = 8.0(2)$ K [7.8(2) K] to the sinusoidal order of the Tb^{3+} spins for TbMn^{16}O$_3$ and TbMn^{18}O$_3$ (in brackets). The transition temperatures, especially of the transition to the ferroelectric/spin-spiral phase, are lower than the previously measured phase transition temperatures in TbMnO$_3$ single crystals, which is in general an indication for the higher quality of single crystal samples [6,16,18].

Remarkably, the magnetic phase transitions for both TbMn^{16}O$_3$ and TbMn^{18}O$_3$ samples occur at almost the same temperatures. This was also observed for oxygen-isotope substituted DyMn$^{16/18}$O$_3$, apart from the ordering temperature of the Dy moments, which showed a significant shift from 7.0(1) K for DyMn^{16}O$_3$ to 5.9(1) K for DyMn^{18}O$_3$ [14]. Oxygen-isotope substitution does not appear to affect the onset of magnetic ordering of the Mn^{3+} spins to the sinusoidal AFM phase or the onset of the multiferroic phase. This result was unexpected since replacing the oxygen-isotope O^{16} by the heavier O^{18} atoms significantly changes the energies of the corresponding lattice vibrations as shown in Fig. 1. This would modify the bond length and Mn-O-Mn bond angles dynamically through the anharmonic lattice potential as in the case of oxygen-isotope substituted DyMn^{18}O$_3$ and DyMn^{16}O$_3$ [14]. As a consequence the NN and NNN exchange interactions J_{ab} and J_b would change as a function of isotope substitution. However, Kimura *et al.* [5] have determined the magnetic phase transition temperatures in the series RMnO$_3$ with R = La-Ho and observed that the magnetic phase transition temperatures of TbMnO$_3$ and DyMnO$_3$ are in a flat minimum when plotted as a function of the Mn-O-Mn bond angles. Therefore, while the exchange energies might be changed by oxygen-isotope substitution, the magnetic phase transition temperatures remain unaltered.

B. Phonon modes of TbMn^{16}O$_3$ and TbMn^{18}O$_3$

TbMnO$_3$ crystallizes in the *Pbnm* space group. The unit cell consists of four formula units, giving TbMnO$_3$ in total 60 phonon modes. The site symmetries of the Tb, Mn, O1, and O2 ions provide an irreducible representation of modes with a total of 24 Raman-active phonons $(7A_g + 7B_{1g} + 5B_{2g} + 5B_{3g})$. Raman spectra of single crystal TbMnO$_3$ samples were acquired in the frequency range from 20 to 700 cm^{-1}. Figure 1 shows the Raman spectra of the O^{16} and O^{18} single-crystal samples of TbMnO$_3$ taken at a temperature of 300 K in parallel $z(xx)\bar{z}$ (A_g modes) and crossed $z(xy)\bar{z}$ (B_{1g} modes) polarization. Within these spectra, five out of seven A_g modes and three out of seven B_{1g} modes are identified. The observed peaks in the Raman spectra are in good agreement with previously published data [43–47]. The two lowest energy A_g modes, which appear at 111.1 cm^{-1} (110.6 cm^{-1}) and 138.5 cm^{-1} (138.8 cm^{-1}) for TbMn^{16}O$_3$ and TbMn^{18}O$_3$ (in brackets) can be attributed to vibrations of the Tb ions within the xy plane. They do not show a shift induced by the oxygen-isotope substitution within the experimental error bar of 0.3 cm^{-1}. The remaining five A_g modes originate from collective in-phase or out-of-phase rotational, bending, and stretching motions of two neighboring MnO$_6$ octahedra that are stacked along the c axis. According to the mode assignment of Iliev *et al.* for the isostructural materials YMnO$_3$ and LaMnO$_3$ given in Ref. [42] and for the series RMnO$_3$ with R = La, Pr, Nd, Sm, Eu, Gd, Tb, Dy, Ho, and Y given in Ref. [43], the peak at 378.2 cm^{-1} (360.0 cm^{-1}) is the $A_g(4)$ mode, which is arising from an out-of-phase octahedral rotation around the z axis. The 488.6 cm^{-1} (464.8 cm^{-1}) $A_g(1)/A_g(3)$ mode is a mixed mode where $A_g(1)$ is an in-phase stretching vibration and $A_g(3)$ is an out-of phase bending vibration of two neighboring MnO$_6$ octahedra, respectively. Due to their close proximity in energy, the strong coupling between the pure $A_g(1)$ and $A_g(3)$ modes results in an anticrossing of both modes with increasing ionic radius of the R ion (i.e., a decrease in the GdFeO$_3$-type distortion in the RMnO$_3$ series [43]) and hence in mixed $A_g(1)/A_g(3)$ and $A_g(3)/A_g(1)$ modes at 488.6 cm^{-1} (464.8 cm^{-1}) and 507.6 cm^{-1} (484.4 cm^{-1}), respectively. It is interesting to note that the mode mixing occurs at the transition from the A-type antiferromagnetic structure to the sinusoidal spin arrangement between Sm and Tb. A similar mixing occurs for the $A_g(2)/A_g(7)$ and $A_g(7)/A_g(2)$ modes, which were too weak to be observed in our Raman light scattering experiments. The $A_g(2)$ mode is an in-phase rotation of two MnO$_6$ octahedra around the z axis and the $A_g(7)$ mode is a motion of the apical oxygen O1 in the y direction. The $B_{1g}(3)$ mode at 472.6 cm^{-1} (452.0 cm^{-1}) can be attributed to an out-of-phase octahedral bending, the $B_{1g}(2)$ mode at 527.7 cm^{-1} (503.4 cm^{-1}) corresponds to an in-plane in-phase O2 scissorlike vibration, and

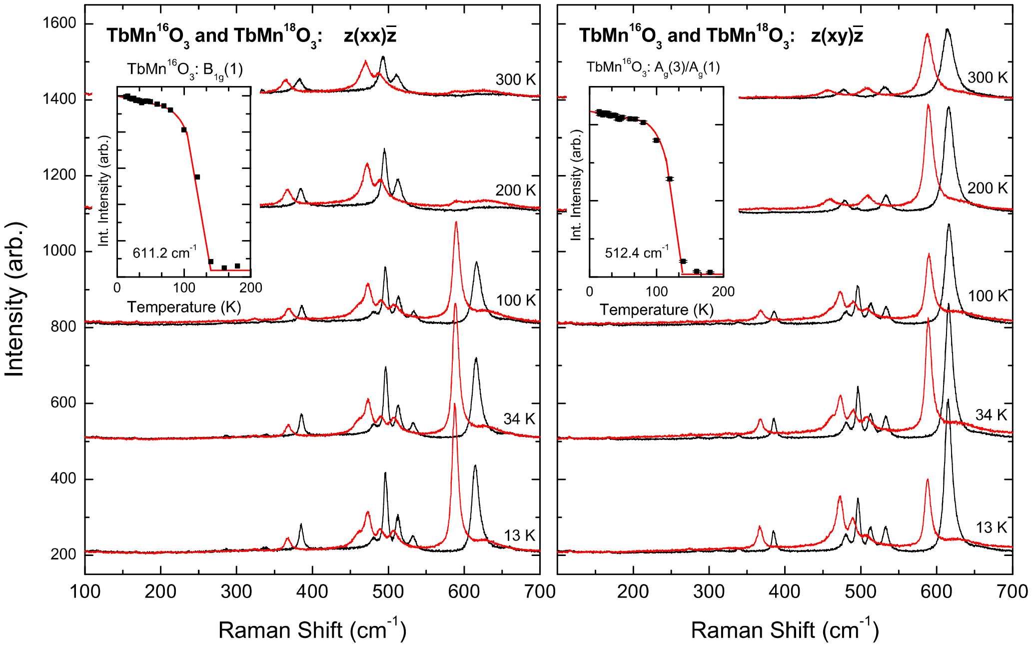

FIG. 3. Raman spectra of the TbMn^{16}O$_3$ (black data) and TbMn^{18}O$_3$ (red data) single crystals at selected temperatures measured in $z(xx)\bar{z}$ (left) and $z(xy)\bar{z}$ (right) polarization. The insets show the temperature dependence of the integrated intensities of the space group *Pbnm* forbidden $B_{1g}(1)$ mode at 614.8 cm^{-1} taken with the $z(xx)\bar{z}$ polarization and the forbidden $A_g(3)/A_g(1)$ mode at 512.4 cm^{-1} taken with the $z(xy)\bar{z}$ polarization for the TbMn^{16}O$_3$ single crystal. The red lines serve as guides to the eye.

the $B_{1g}(1)$ mode at 610.6 cm^{-1} (582.8 cm^{-1}) is described by an in-plane, in-phase octahedral stretching motion. The (anti)stretching $A_g(3)/A_g(1)$, $A_g(1)/A_g(3)$, and $B_{1g}(1)$ modes are also Jahn-Teller active [43,48,49]. Therefore, these vibrational modes are particularly sensitive to changes within the MnO$_6$ crystal-field environment.

According to Iliev *et al.* [50,51] the additional peak at $\approx$640 cm^{-1} cannot be assigned to a regular phonon mode. Rather, it originates from zone boundary phonon contributions; particularly from oxygen vibrations. They become Raman active through defect induced breaking of the translational symmetry. The Raman experiments of Iliev *et al.* show that the intensity of this mode changes for different samples [50,51]. In our Raman measurements the relative intensity of this mode, which possesses two pronounced shoulders at 614.0 cm^{-1} (584.1 cm^{-1}) and 648.2 cm^{-1} (621.2 cm^{-1}) in TbMn^{16}O$_3$ (TbMn^{18}O$_3$) varies with the position of the laser spot on the sample. This is an indication that this mode is activated by surface defects.

C. Temperature induced phonon anomalies

The temperature dependence of the Raman spectra of the TbMn^{16}O$_3$ and TbMn^{18}O$_3$ single crystals were measured in parallel $z(xx)\bar{z}$ and crossed $z(xy)\bar{z}$ polarization conditions in the temperature range from 13 to 300 K (see Fig. 3). Pronounced changes in the intensities of selected phonon modes appear in both polarization $z(xx)\bar{z}$ and $z(xy)\bar{z}$ spectra at around 140 K. At this temperature additional modes appear in parallel and crossed polarization. The modes in parallel polarization can be attributed to formerly forbidden B_{1g} modes and the modes in crossed polarization to forbidden A_g modes for the space group *Pbnm* for the corresponding polarization. The insets in Fig. 3 show the rapid increases of the integrated intensities of the $B_{1g}(1)$ mode at 614.8 cm^{-1} in the $z(xx)\bar{z}$ configuration and the $A_g(1)/A_g(3)$ mode at 512.4 cm^{-1} in the $z(xy)\bar{z}$ configuration for the TbMn^{16}O$_3$ single crystal. Such a behavior is characteristic for a change in crystal symmetry. In their x-ray powder diffraction experiments Agarwal *et al.* have determined that the crystal structure of TbMnO$_3$ is lowered from *Pbnm* at 300 K to one of the polar space groups $Pn2_1a$ or $P2_1ma$ [52] at a temperature of 2 K. However, for both proposed space groups the Raman selection rule for the used polarizations in Fig. 3 are not correct. The point groups $C_1(1)$, $C_i(-1)$, and $C_{2h}(2m)$ would allow for the appearance of the formerly forbidden B_{1g} modes in parallel polarization $z(xx)\bar{z}$ and the A_g modes in crossed polarization $z(xx)\bar{z}$. Among the possible subgroups of *Pbnm* (No. 62), two monoclinic space groups possess the required point group, namely, $P2_1/m$ (No. 11) and $P2_1/c$ (No. 14) which belong to the point group $C_{2h}(2/m)$. Both space groups are centrosymmetric and would therefore not be ferroelectric. However, a further lowering of the crystal symmetry cannot be ruled out and more detailed experiments, using for example high resolution diffraction techniques, are required.

Figure 4 presents the frequencies and linewidth (full width at half maximum, FWHM), as determined by fitting Voigt profiles to the experimental data, for the three most prominent modes: the $A_g(4)$ mode at 381.12(7) cm^{-1} (362.9(2) cm^{-1}), the $A_g(1)/A_g(3)$ at 492.37(7) cm^{-1} (468.38(8) cm^{-1}), and the $B_{1g}(1)$ mode at 611.22(7) cm^{-1} (583.4(2) cm^{-1}) for TbMn^{16}O$_3$ and TbMn^{18}O$_3$ (in brackets), respectively. The given phonon frequencies correspond to the values obtained at 13 K. The dotted vertical lines in Figs. 4 and 5 correspond to the magnetic and ferroelectric phase transition temperatures obtained on single-crystal TbMnO$_3$ [16]. For temperatures

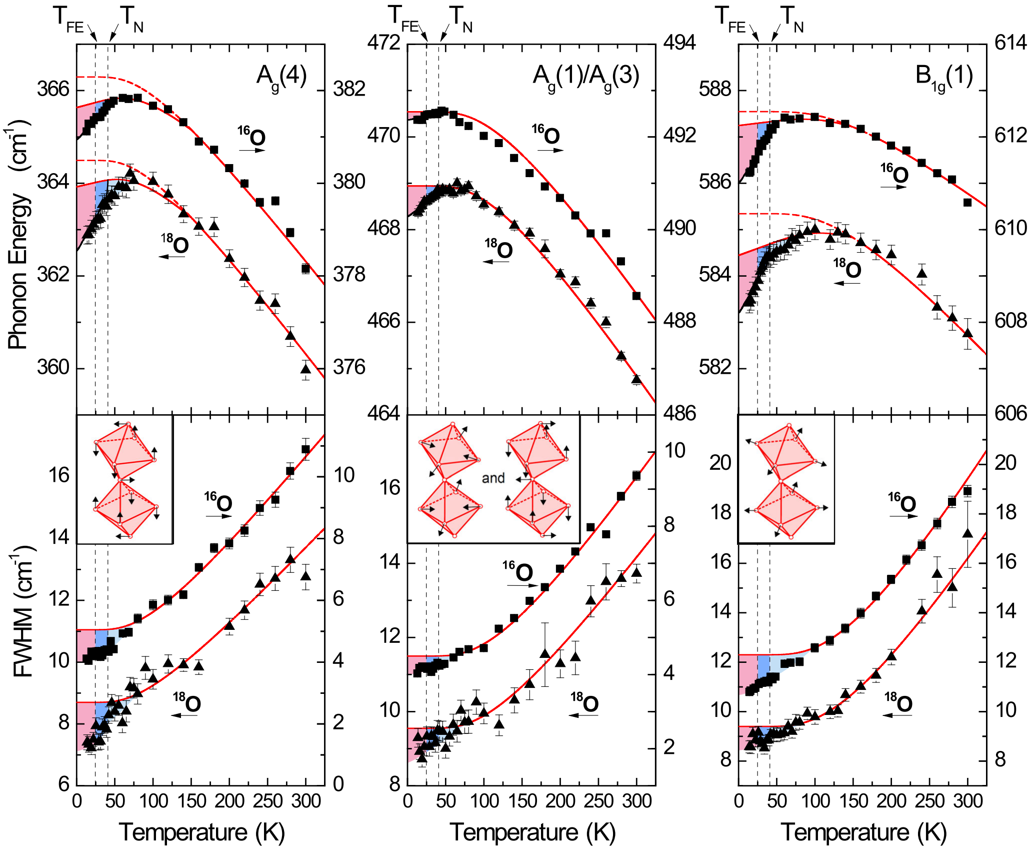

FIG. 4. Temperature dependence of the phonon energies (upper panels) and linewidth (lower panels) of the $A_g(4)$, $A_g(1)/A_g(3)$, and $B_{1g}(1)$ modes for single-crystal TbMn^{16}O$_3$ and TbMn^{18}O$_3$. Note, the data of the two samples were shifted for a better presentation. The phase transition temperatures $T_N^{\mathrm{Mn}} = 41$ K and $T_{\mathrm{FE}} = 28$ K as given by Kenzelmann *et al.* in Ref. [16] are marked as vertical dashed lines. The dashed red lines represent the calculated temperature dependence of peak positions and linewidth where only anharmonic phonon-phonon interactions are considered [Eqs. (1) and (2)]. For the solid red lines the additional shift caused by the anisotropic thermal expansion of the crystal lattice, which starts at about 140 K, were also taken into account. The red and blue areas indicate the additional shifts below the magnetic and multiferroic phase transitions.

above ~100 K the phonons shift to lower frequencies (ω_{ph}) and their linewidth (Γ_{ph}) increases. This is caused by anharmonic phonon-phonon interactions, i.e., the decay of an optical phonon into two phonons of lower energy [53]. In the first approximation a symmetric decay into two phonons with the same energy, i.e., $\omega_0/2$ of the initial optical phonon, can be considered (Klemens decay [54]). The resulting shift and line broadening can be expressed as [55,56]

$$\omega_{\mathrm{ph}}(T) = -\omega^0_{\mathrm{anh.}}\left(1 + \frac{2}{\exp(\hbar\omega_0/2k_{\mathrm{B}}T) - 1}\right) + \omega_0, \qquad (1)$$

$$\Gamma_{\mathrm{ph}}(T) = \Gamma^0_{\mathrm{anh.}}\left(1 + \frac{2}{\exp(\hbar\omega_0/2k_{\mathrm{B}}T) - 1}\right) + \Gamma_0, \qquad (2)$$

where the parameters $\omega^0_{\mathrm{anh.}}$ and $\Gamma^0_{\mathrm{anh.}}$ are positive constants arising from the matrix element of the phonon-phonon interaction. The temperature induced shift and line broadening correspond to the real and imaginary parts of the phonon self-energy and are coupled through the Kramers-Kronig relation. In Fig. 4 the dashed red lines indicate the fits of Eqs. (1) and (2) to the experimental data for the temperature range between 100 and 300 K, where the intrinsic phonon frequency ω_0 was taken as a fixed parameter for both the change in frequency and the linewidth.

Additional shifts in the phonon energies from the expected anharmonic behavior occur below about 140 K. This effect is particularly apparent in Fig. 4 for the $A_g(4)$ and $B_{1g}(1)$ modes. Similar behavior has been observed for DyMnO$_3$ [44,57] and also by Mansouri *et al.* for TbMnO$_3$ [47].

Measurements of the thermal expansion of TbMnO$_3$ [58] indicate that at about 140 K the lattice parameters change, where the expansion of the a axis is compensated by a contraction of the b axis with decreasing temperature. This anisotropic thermal expansion is caused by additional tilts and distortions of the MnO$_6$ octahedra. Depending on the atomic displacements, the corresponding phonon modes are affected by these lattice distortions. We have qualitatively modeled the phonon frequency shifts within the framework of the Grüneisen parameter $\gamma_{i\mathbf{q}} = \frac{B_0}{\omega_{i\mathbf{q}}}\frac{\partial\omega_{i\mathbf{q}}}{\partial P}$, where B_0 is the bulk compressibility and $\frac{\partial\omega_{i\mathbf{q}}}{\partial P}$ is the change in frequency of a particular phonon with pressure P. The corresponding shift in phonon frequency as a function of the change in volume is $(\Delta\omega_i)_{\mathrm{latt.}} = -\gamma_i\omega_i\frac{\Delta V}{V}$. The Grüneisen parameters for RMnO$_3$ with $R =$ Dy, Gd, Eu, Sm, and Pr have been determined

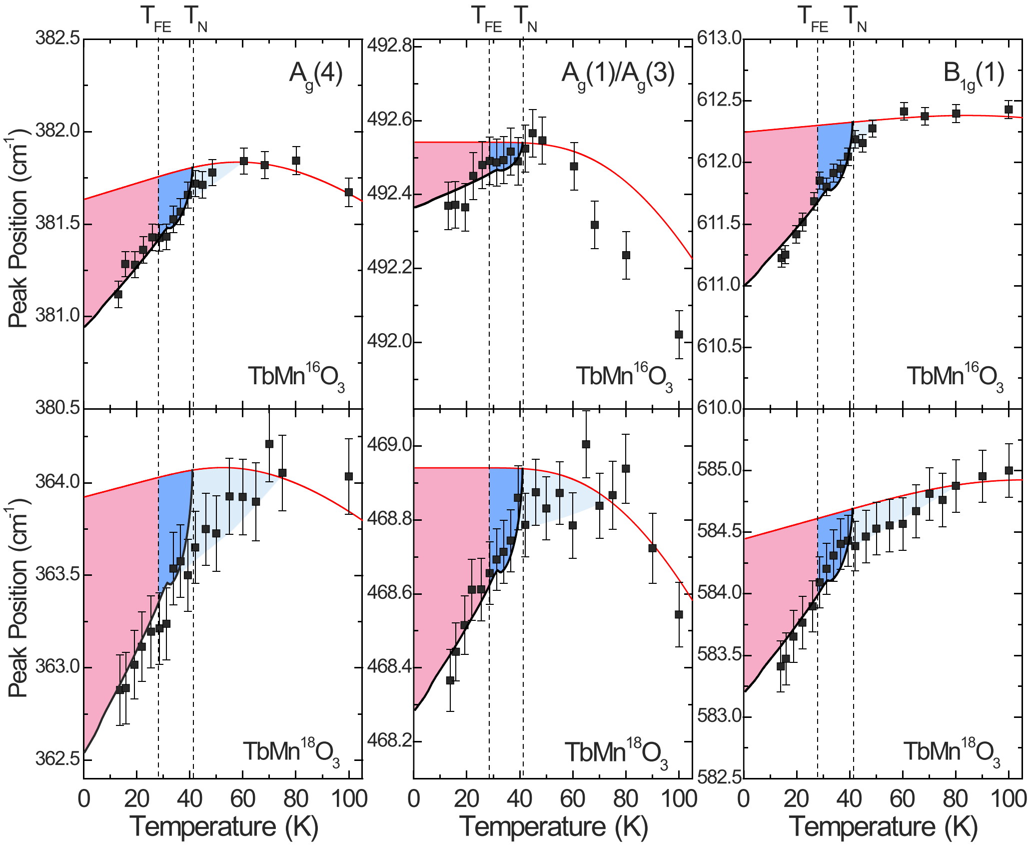

FIG. 5. Temperature dependence of the phonon frequency of the $A_g(4)$, $A_g(1)/A_g(3)$, and $B_{1g}(1)$ modes for single-crystal $\mathrm{TbMn^{16}O_3}$ and $\mathrm{TbMn^{18}O_3}$ in the temperature range from 13 to 100 K. The vertical dashed lines correspond to the antiferromagnetic and multiferroic phase transitions at $T_N^{\mathrm{Mn}} = 41$ K and $T_{\mathrm{FE}} = 28$ K, as taken from Ref. [16], respectively. The red line corresponds to temperature dependence of the phonon frequency in the case of anharmonic phonon-phonon interactions, where effects arising from the anisotropic thermal expansion were also taken into account. The red and dark-blue areas mark the additional changes below the sinusoidal AFM and multiferroic phase transitions and the light-blue area indicates the start of the phonon anomalies which occurs already 20 K above the magnetic phase transition. The black line is the fit of the effect of the spin-phonon coupling using Eq. (5) to the experimental data.

experimentally by Mota *et al.* [59]. By interpolating their data to $\mathrm{TbMnO_3}$, the Grüneisen parameter for the $A_g(4)$ mode is $\gamma \approx 1.35$ and for the $B_{1g}(1)$ mode is $\gamma \approx 0.98$. Using the anisotropic thermal expansion determined by Meier *et al.* [58], we have calculated the addition phonon shift and have added it to the temperature induced shift caused by the anharmonic phonon-phonon decay (see red solid lines in Figs. 4 and 5).

Below the magnetic phase transition at $T_N^{\mathrm{Mn}} = 41$ K and below the multiferroic phase transition at $T_{\mathrm{FE}} = 28$ K [16], additional shifts in the phonon energies and linewidth occur. This is indicated by the dark red and dark blue areas in Figs. 4 and 5, which provides a closer examination of the mode frequencies below 100 K. The most pronounced changes appear below the magnetic transition into the sinusoidal phase at $T_N^{\mathrm{Mn}} = 41$ K (dark-blue areas). At this transition the phonon energies soften and the phonon linewidths decrease. An additional change in the rate of the phonon softening is observed at the phase transition to the *bc*-spin-spiral/ferroelectric phase at $T_{\mathrm{FE}} = 28$ K, as indicated by the red areas. This is most pronounced for the $A_g(1)/A_g(3)$ and $B_{1g}(1)$ modes. Similar shifts also occur for the $A_g(3)/A_g(1)$ and $B_{1g}(2)$ modes (data not shown here). Previously, Laverdière *et al.* have measured the temperature dependence of the Raman spectrum of $R\mathrm{MnO_3}$ with $R =$ Pr, Nd, Sm, Eu, Gd, Tb, Dy, Ho, and Y [44] and measured pronounced shifts in the phonon frequencies of, for example, the $B_{1g}(1)$ and $A_g(1)/A_g(3)$ modes for the manganates with $R =$ Pr, Nd, Sm, and Dy, but no shifts were observed for the compounds with $R =$ Eu, Gd, Tb, Ho, and Y. However, Rovillain *et al.* [48,49] and Mansouri *et al.* [47] observed weak phonon shifts below the magnetic phase transitions in the Raman spectrum of $\mathrm{TbMnO_3}$. Infrared measurements performed by Schmidt *et al.* [60] and Schleck *et al.* [61] demonstrated that the IR-active B_{1u}, B_{2u}, and B_{3u} modes also possess additional phonon shifts in the magnetically ordered phases.

The phonon renormalizations observed for the $A_g(4)$, $A_g(1)/A_g(3)$, and $B_{1g}(1)$ modes are likely not the result of electron-phonon interactions. $\mathrm{TbMnO_3}$ remains an insulator down to lowest temperatures, and there are no indications for a phonon asymmetry caused by a Fano peak profile, nor of a transfer of intensity within the spectral background. This leaves structural and/or magnetic effects as the main considerations for the mode anomalies within the magnetic and multiferroic phases at low temperatures. A possible origin for the change in mode energies could be the effect of magnetostriction. At the onset of the magnetic order the spin exchange energy can alter the interatomic potential between bonded ions and hence change the atomic distances, as observed in $DyMn^{16}O_3$ and its oxygen-isotope substituted counterpart $DyMn^{18}O_3$ [14]. The additional shift in phonon frequency with temperature is then proportional to the spin-correlation function $\langle \mathbf{S}_i \cdot \mathbf{S}_j \rangle$. However, the experimentally determined changes in atomic distances at the magnetic phase transitions are in the subpicometer range, i.e., below 0.5×10^{-12} m [12–14]. Therefore, the expected change in the interatomic potential is too small to account for the observed phonon shifts. Furthermore, the change in linewidth below the magnetic phase transitions cannot be explained with a spin-lattice coupling effect since it would require a significant change in the two-phonon density of states.

These considerations leave the spin-phonon interaction as the most likely effect causing the observed phonon anomalies in the magnetically ordered phases. Lattice vibrations modify the exchange integral through the modulation of Mn-O bond length and Mn-O-Mn bond angles, which modulate the orbital overlap between the ions. The change in the exchange interaction J_{ij}, caused by the lattice vibration of the αth phonon mode, can be calculated through a Taylor expansion of J_{ij} with respect to the displacement vector $\boldsymbol{u}_k^\alpha(t)$ of the contributing ion [35,36]:

$$\Delta J_{ij}^\alpha\big(\mathbf{u}_k^\alpha(t)\big) = \big[\mathbf{u}_k^\alpha(t) \cdot \nabla_k\big] J_{ij} + \tfrac{1}{2}\big[\mathbf{u}_k^\alpha(t) \cdot \nabla_k\big]^2 J_{ij} + \cdots . \tag{3}$$

The first (linear) term corresponds to a static lattice deformation and does not contribute to the temperature dependence of the lattice vibration. Third- and higher-order (anharmonic) terms would be substantially smaller and can be neglected in the current approximation. Shifts in phonon frequency due to coupling with the magnetic system are mainly caused by the quadratic term and the corresponding shift in phonon frequency can be expressed as [36]

$$(\Delta\omega_\alpha)_{\text{s-ph}} = \frac{N}{2\mu_\alpha\omega_\alpha} \sum_k \langle \mathbf{S}_i \cdot \mathbf{S}_j \rangle_k \big[\hat{\mathbf{u}}_k^\alpha(t) \cdot \nabla_k\big]^2 J_k, \tag{4}$$

where μ_α is the reduced mass of the atoms which are participating in the vibration, N is the number of Mn^{3+} ions per unit cell, and $\hat{\boldsymbol{u}}_k^\alpha = \mathbf{u}_k^\alpha / |\mathbf{u}_k^\alpha|$ is the direction of the phonon displacement. The spin-correlation function $\langle \mathbf{S}_i \cdot \mathbf{S}_j \rangle$ is temperature dependent and can be expressed by the magnetization of the Mn^{3+} sublattice $[M_{Mn}(T)]^2$. The sign of the spin-phonon coupling determines whether a phonon mode softens or hardens below the magnetic phase transition temperature, and depends on the sign of the spin-spin exchange interaction in the direction of the atomic displacement.

Laverdière *et al.* [44] extended these considerations in order to account for competing spin-spin interactions in an incommensurate magnetic structure. For a sinusoidal or spin-spiral phase with a propagation vector of the spin modulation along the b axis $(0, k_y, 0)$, as in $TbMnO_3$, the spin correlation function is given by $\langle \mathbf{S}_i \cdot \mathbf{S}_{i+r} \rangle = K(T)\cos(2\pi \mathbf{k}_y \cdot \mathbf{r})$, where $K(T) = (M_{\mathrm{Mn}}/4\mu_B)^2$ and $2\pi \mathbf{k}_k \cdot \mathbf{r}$ is the spin canting angle between two neighboring Mn^{3+} sites. In the case of competing NN and NNN spin interactions, the induced frequency shift of a phonon mode is then given by

$$\Delta\omega_\alpha = \frac{K(T)}{\mu_\alpha\omega_0}[2D_1\cos(\pi k_y) + D_2\cos(2\pi k_y) + D_3], \tag{5}$$

where the strength of spin-phonon coupling for an incommensurate spin structure is strongly dependent on the length of the propagation vector k_y as well as the relative strengths of D_1, D_2, and D_3 [44].

In order to explain the observed shifts in phonon frequency below $T_{\mathrm{N}}^{\mathrm{Mn}} = 41$ K, we have applied the model of spin-phonon interactions and have fitted Eq. (5) to the experimental data. For the temperature dependence of the length of the magnetic propagation vector k_y we have used the data of Kenzelmann *et al.* [16] as input parameter. $K(T)$ is proportional to $[\mathbf{M(T)}]^2$. Given that the intensity of a magnetic Bragg reflection is proportional to $[\mathbf{M(T)}]^2$, we have calculated the spin-phonon coupling by taking the intensity of the $(0\ k_y\ 1)$ magnetic Bragg peak from Ref. [16]. A good agreement to the experimental data was obtained for a $D_1{:}D_2$ ratio of 1 : 28 simultaneously for all three phonon modes. The parameter D_3 did not play a role and was not taken into account. Using this ratio, the phonon shift below $T_{\mathrm{N}}^{\mathrm{Mn}} = 41$ K and the change in slope of the temperature dependence of the phonon frequency at around the phase transition from the sinusoidal to the bc plane spin spiral at $T \sim 30$ K is well reproduced (see red and dark-blue areas in Figs. 4 and 5). Since at the transition at 28 K no change in the ratio of $D_1{:}D_2$ is required, the observed changes in phonon frequency and linewidth are entirely arising from the temperature dependence of k_y, which decreases linearly with decreasing temperature in the sinusodial phase and remains almost constant below about 30 K, with only a small variation [16]. The fact that the same $D_1{:}D_2$ ratio was obtained for all investigated phonons shown in Figs. 4 and 5 and for the $A_g(3)/A_g(1)$ mode at 512.4 (489.2 cm^{-1}) (data not shown here) confirms the robustness of the used model for the spin-phonon interaction. Note that D_2 [see second term in Eq. (5)] can be referred to the next-nearest neighbor interaction, which is a leading contribution for the formation of the incommensurate spin-spiral phase. The $A_g(4)$, $A_g(1)/A_g(3)$, and $B_{1g}(1)$ modes involve MnO_6 stretching and bending motions that modulate the Mn-O bond lengths and Mn-O-Mn bond angles within the ab plane. The spin induced phonon softening observed for these modes thus reflects the modulation of both the J_{ab} and J_b exchange interactions in the ab plane. Since the AFM order along the c axis does not change, the spin-phonon coupling effects must exclusively pertain to the ab plane. This is of particular importance for the $B_{1g}(1)$ mode, which shows the strongest shift in phonon frequency despite the $1/\omega_0$ dependence of the spin-phonon coupling [see Eq. (5)].

Although the above given derivation of the spin-phonon interaction is semiclassical, the self-energy related to the spin-phonon interaction is based on a microscopic quantum-mechanical effect. The real part (phonon shifts) and imaginary part (linewidth) of the phonon self-energy are coupled through the Kramers-Kronig relation. Therefore, a shift in phonon frequency must be associated with a change in the phonon lifetime. Such changes in linewidth are present below $T_{\mathrm{N}}^{\mathrm{Mn}} = 41$ K, as shown in Fig. 4. This serves as further evidence that the changes in phonon frequency and linewidth below the magnetic phase transition are caused by spin-phonon renormalization effects and not through atomic displacements.

Small phonon shifts are already observed in the paramagnetic phase at temperatures of about 10–20 K above the onset of magnetic order (see light-blue areas in Figs. 4 and 5). In this temperature range, short-range, short-lifetime correlations already form between fluctuating spins $\Delta\mathbf{S}_i$ and $\Delta\mathbf{S}_j$ at neighboring Mn^{3+} sites [62]. This affects the spin-spin correlation function $\langle \Delta\mathbf{S}_i \cdot \Delta\mathbf{S}_j \rangle$ and is consequently manifested in an early onset of the renormalizations of phonon energies and lifetimes. Similar behavior has also been observed for *A*-type AFM manganites [36,44].

For the two oxygen-isotope substituted $TbMnO_3$ samples, differences in the phonon behaviors are observed. In the temperature range between 50 and 300 K, both the changes in phonon energy and linewidth of the $TbMn^{16}O_3$ and $TbMn^{18}O_3$ are almost identical. However, the spin induced renormalizations are more pronounced for the O^{18} substituted sample. This holds for both transitions, the transition to the sinusoidal spin phase at 41 K and the transition to the ferroelectric/spin-spiral phase at 28 K. This demonstrates the strong involvement of the oxygen ions in the spin-phonon coupling. The mass of the oxygen ions is included in Eq. (5) directly through the effective mass μ_α and indirectly through the phonon frequency ω_α, which is proportional to $\sqrt{k/\mu_\alpha}$. According to this consideration, the effect of the spin-phonon coupling should be more pronounced for the $TbMn^{16}O_3$ sample, which was not observed. Nevertheless, the fitting of Eq. (5) to the experimental data of the phonon shift with temperature gave the same $D_1{:}D_2$ ratio of 1 : 28 for both oxygen-isotope pure samples, i.e., the ratio between the NN and NNN magnetic exchange interactions does not change upon oxygen-isotope substitution. This is further supported by the neutron diffraction data on $DyMnO_3$, where oxygen-isotope substitution also did not affect the magnetic propagation vector [14].

IV. CONCLUSIONS

We have investigated the effect of the oxygen-isotope substitution on $TbMnO_3$ with respect to its magnetic and ferroelectric properties. Even so that the energy of the phonon modes changes significantly with oxygen-isotope substitution, heat capacity measurements on powder O^{16} and O^{18} substituted samples reveal no significant changes in phase transition temperatures to the spin-sinusoidal and ferroelectric/spin-spiral phases. This indicates that a dynamical modulation of the distortion of the MnO_6 octahedra or the modulation of the Mn-O-Mn bond angle has no influence on the magnetic properties of $TbMnO_3$ and can be explained with the fact that changes in the Mn-O-Mn bond angle hardly affects the magnetic phase transition temperatures in $TbMnO_3$ [19]. The phonon behaviors of the O^{16} and O^{18} substituted single-crystal $TbMnO_3$ samples were measured by Raman light scattering as a function of temperature. Additional phonon modes were observed at 140 K. This could indicate the breaking of the crystal symmetry. Deviations from the expected temperature dependence arising from anharmonic phonon-phonon interactions and the anisotropic thermal expansion of $TbMnO_3$ occur below both the *b*-sinusoidal and *bc*-spin-spiral AFM phase transitions at 41 and 28 K, respectively. We have determined that the observed mode softening and decreased linewidths at both phase transitions are the result of spin-phonon interactions induced by phonon coupling to the magnetic exchange interactions within the *ab* plane, where the leading term is the next-nearest-neighbor interactions. No further mechanisms, which would involve for example atomic displacements upon entering the ferroelectric phase at 28 K, or effects arising from the formation of the electromagnon are required. These observations further support the spin-current model as the main mechanism for the electromagnetic coupling in $TbMnO_3$.

ACKNOWLEDGMENTS

We would like to thank C. D. Ling for the use of the PPMS for heat capacity measurements at the School of Chemistry, University of Sydney. This work was supported through the Australian Institute of Nuclear Science and Engineering Ltd. (AINSE) and the Australian Research Council (ARC) through the funding of the Discovery Grants No. DP110105346 and No. DP160100545.

---

[1] N. Hur, S. Park, P. A. Sharma, J. S. Ahn, S. Guha, and S-W. Cheong, Electric polarization reversal and memory in a multiferroic material induced by magnetic fields, Nature (London) **429**, 392 (2004).

[2] W. Eerenstein, N. D. Mathur, and J. F. Scott, Multiferroic and magnetoelectric materials, Nature (London) **442**, 759 (2006).

[3] S.-W. Cheong and M. Mostovoy, Multiferroics: A magnetic twist for ferroelectricity, Nat. Mater. **6**, 13 (2007).

[4] Y. Tokura, S. Seki, and N. Nagaosa, Multiferroics of spin origin, Rep. Prog. Phys. **77**, 076501 (2014).

[5] T. Kimura, T. Goto, H. Shintani, K. Ishizaka, T. Arima, and Y. Tokura, Magnetic control of ferroelectric polarization, Nature (London) **426**, 55 (2003).

[6] T. Goto, T. Kimura, G. Lawes, A. P. Ramirez, and Y. Tokura, Ferroelectricity and Giant Magnetocapacitance in Perovskite Rare-Earth Manganites, Phys. Rev. Lett. **92**, 257201 (2004).

[7] M. Gajek, M. Bibes, S. Fusil, K. Bouzehouane, J. Fontcuberta, A. Barthelemy, and A. Fert, Tunnel junctions with multiferroic barriers, Nat. Mater. **6**, 296 (2007).

[8] C.-W. Nan, M. I. Bichurin, S. Dong, D. Viehland, and G. Srinivasan, Multiferroic magnetoelectric composites: Historical perspective, status, and future directions, J. Appl. Phys. **103**, 031101 (2008).

[9] J. F. Scott, Multiferroic memories, Nat. Mater. **6**, 256 (2007).

[10] I. A. Sergienko and E. Dagotto, Role of the Dzyaloshinskii-Moriya interaction in multiferroic perovskites, Phys. Rev. B **73**, 094434 (2006).

[11] H. Katsura, N. Nagaosa, and A. V. Balatsky, Spin Current and Magnetoelectric Effect in Noncollinear Magnets, Phys. Rev. Lett. **95**, 057205 (2005).

[12] H. C. Walker, F. Fabrizi, L. Paolasini, F. de Bergevin, J. Herrero-Martin, A. T. Boothroyd, D. Prabhakaran, and D. F. McMorrow, Femtoscale magnetically induced lattice distortions in multiferroic $TbMnO_3$, Science **333**, 1273 (2011).

[13] H. C. Walker, F. Fabrizi, L. Paolasini, F. de Bergevin, D. Prabhakaran, A. T. Boothroyd, and D. F. McMorrow, Circularly polarized x-ray scattering investigation of spin-lattice coupling

in $TbMnO_3$ in crossed electric and magnetic fields, Phys. Rev. B **88**, 214415 (2013).

[14] N. Narayanan, P. J. Graham, N. Reynolds, F. Li, P. Rovillain, J. Hester, J. Kimpton, M. Yethiraj, G. J. McIntyre, W. D. Hutchison, and C. Ulrich, Subpicometer-scale atomic displacements and magnetic properties in the oxygen-isotope substituted multiferroic $DyMnO_3$, Phys. Rev. B **95**, 075154 (2017).

[15] *International Tables for Crystallography, Volume A1, Symmetry Relations Between Space Groups*, edited by Hans Wondratschek and Ulrich Müller (Kluwer Academic, Dordrecht/Boston/London, 2004).

[16] M. Kenzelmann, A. B. Harris, S. Jonas, C. Broholm, J. Schefer, S. B. Kim, C. L. Zhang, S. W. Cheong, O. P. Vajk, and J. W. Lynn, Magnetic Inversion Symmetry Breaking and Ferroelectricity in $TbMnO_3$, Phys. Rev. Lett. **95**, 087206 (2005).

[17] S. Quezel, F. Tcheou, J. Rossat-Mignod, G. Quezel, and E. Roudaut, Magnetic structure of the perovskite-like compounds $TbMnO_3$, Physica (B+C) **86–88**, 916 (1977).

[18] R. Kajimoto, H. Yoshizawa, H. Shintani, T. Kimura, and Y. Tokura, Magnetic structure of $TbMnO_3$ by neutron diffraction, Phys. Rev. B **70**, 012401 (2004).

[19] T. Kimura, S. Ishihara, H. Shintani, T. Arima, K. T. Takahashi, K. Ishizaka, and Y. Tokura, Distorted perovskite with e_g^1 configuration as a frustrated spin system, Phys. Rev. B **68**, 060403(R) (2003).

[20] O. Prokhnenko, R. Feyerherm, M. Mostovoy, N. Aliouane, E. Dudzik, A. U. B. Wolter, A. Maljuk, and D. N. Argyriou, Coupling of Frustrated Ising Spins to the Magnetic Cycloid in Multiferroic $TbMnO_3$, Phys. Rev. Lett. **99**, 177206 (2007).

[21] T. Arima, T. Goto, Y. Yamasaki, S. Miyasaka, K. Ishii, M. Tsubota, T. Inami, Y. Murakami, and Y. Tokura, Magnetic-field-induced transition in the lattice modulation of colossal magnetoelectric $GdMnO_3$ and $TbMnO_3$ compounds, Phys. Rev. B **72**, 100102(R) (2005).

[22] J.-S. Zhou and J. B. Goodenough, Unusual Evolution of the Magnetic Interactions versus Structural Distortions in $R$$MnO_3$ Perovskites, Phys. Rev. Lett. **96**, 247202 (2006).

[23] M. Mochizuki and N. Furukawa, Microscopic model and phase diagrams of the multiferroic perovskite manganites, Phys. Rev. B **80**, 134416 (2009).

[24] C. A. Reynolds, B. Serin, W. H. Wright, and L. B. Nesbitt, Superconductivity of Isotopes of Mercury, Phys. Rev. **78**, 487 (1950).

[25] E. Maxwell, Isotope Effect in the Superconductivity of Mercury, Phys. Rev. **78**, 477 (1950).

[26] B. Batlogg, G. Kourouklis, W. Weber, R. J. Cava, A. Jayaraman, A. E. White, K. T. Short, L. W. Rupp, and E. A. Rietman, Nonzero Isotope Effect in $La_{1.85}Sr_{0.15}CuO_4$, Phys. Rev. Lett. **59**, 912 (1987).

[27] H.-C. Z. Loye, K. J. Leary, S. W. Keller, W. K. Ham, T. A. Faltens, J. N. Michaels, and A. M. Stacy, Oxygen isotope effect in high-temperature oxide superconductors, Science **238**, 1558 (1987).

[28] M. Cardona, R. Liu, C. Thomsen, W. Kress, E. Schonherr, M. Bauer, L. Genzel, and W. König, Effect of isotopic substitution of oxygen on T_c and the phonon frequencies of high T_c superconductors, Solid State Commun. **67**, 789 (1988).

[29] C. Thomson, H. Mattausch, M. Bauer, W. Bauhofer, R. Liu, L. Genzel, and M. Cardona, Raman and far infrared studies of $YBa_2Cu_3O_{7-\delta}$ prepared exclusively with O^{18}, Solid State Commun. **67**, 1069 (1988).

[30] S. Hoen, W. N. Creager, L. C. Bourne, M. F. Crommie, T. W. Barbee III, Marvin L. Cohen, A. Zettl, L. Bernardez, and J. Kinney, Oxygen isotope study of $YBa_2Cu_3O_7$, Phys. Rev. B **39**, 2269 (1989).

[31] N. A. Babushkina, A. N. Taldenkov, E. A. Chistotina, A. V. Inyushkin, O. Y. Gorbenko, A. R. Kaul, K. I. Kugel, and D. I. Khomskii, The effect partial isotope substitution O^{16}–O^{18} on physical properties of La–Pr manganites, J. Magn. Magn. Mater. **242-245**, 640 (2002).

[32] M. Itoh, R. Wang, Y. Inaguma, T. Yamaguchi, Y.-J. Shan, and T. Nakamura, Ferroelectricity Induced by Oxygen Isotope Exchange in Strontium Titanate Perovskite, Phys. Rev. Lett. **82**, 3540 (1999).

[33] M. Bartkowiak, G. J. Kearley, M. Yethiraj, and A. M. Mulders, Symmetry of ferroelectric phase of $SrTi^{18}O_3$ determined by *ab initio* calculations, Phys. Rev. B **83**, 064102 (2011).

[34] S. E. Rowley, L. J. Spalek, R. P. Smith, M. P. M. Dean, M. Itoh, J. F. Scott, G. G. Lonzarich, and S. S. Saxena, Ferroelectric quantum criticality, Nat. Phys. **10**, 367 (2014).

[35] W. Baltensperger and J. S. Helman, Influence of magnetic order in insulators on the optical phonon frequency, Helv. Phys. Acta **41**, 668 (1968).

[36] E. Granado, A. García, J. A. Sanjurjo, C. Rettori, I. Torriani, F. Prado, R. D. Sánchez, A. Caneiro, and S. B. Oseroff, Magnetic ordering effects in the Raman spectra of $La_{1-x}Mn_{1-x}O_3$, Phys. Rev. B **60**, 11879 (1999).

[37] A. S. Barker, Jr. and R. Loudon, Response functions in the theory of Raman scattering by vibrational and polariton modes in dielectric crystals, Rev. Mod. Phys. **44**, 18 (1972).

[38] M. D. Fontana, H. Idrissi, G. E. Kugel, and K. Wojcik, Raman spectrum in $PbTiO_3$, re-examined: Dynamics of the soft phonon and the central peak, J. Phys.: Condens. Matter **3**, 8695 (1991).

[39] A. A. Sirenko, C. Bernhard, A. Golnik, Anna M. Clark, Jianhua Hao, W. Si, and X. X. Xi, Soft-mode hardening in $SrTiO_3$ thin films, Nature (London) **404**, 373 (2000).

[40] F. Widulle, J. Serrano, and M. Cardona, Disorder-induced phonon self-energy of semiconductors with binary isotopic composition, Phys. Rev. B **65**, 075206 (2002).

[41] V. A. Trepakov, A. G. Dejneka, O. E. Kvyatkovskii, D. Chvostova, Z. Potucek, M. E. Savinov, L. Jastrabik, X. Wang, and S.-W. Cheong, Electronic structure, optical and dielectric spectroscopy study of $TbMnO_3$, arXiv:1604.02428v3.

[42] M. N. Iliev, M. V. Abrashev, H.-G. Lee, V. N. Popov, Y. Y. Sun, C. Thomsen, R. L. Meng, and C. W. Chu, Raman spectroscopy of orthorhombic perovskitelike $YMnO_3$ and $LaMnO_3$, Phys. Rev. B **57**, 2872 (1998).

[43] M. N. Iliev, M. V. Abrashev, J. Laverdière, S. Jandl, M. M. Gospodinov, Y.-Q. Wang, and Y.-Y. Sun, Distortion-dependent Raman spectra and mode mixing in $R$$MnO_3$ perovskites ($R =$ La, Pr, Nd, Sm, Eu, Gd, Tb, Dy, Ho, Y), Phys. Rev. B **73**, 064302 (2006).

[44] J. Laverdière, S. Jandl, A. A. Mukhin, V. Yu. Ivanov, V. G. Ivanov, and M. N. Iliev, Spin-phonon coupling in orthorhombic $R$$MnO_3$ ($R =$ Pr, Nd, Sm, Eu, Gd, Tb, Dy, Ho, Y): A Raman study, Phys. Rev. B **73**, 214301 (2006).

[45] P. Kumar, S. Saha, D. V. S. Muthu, J. R. Sahu, K. Sood, and C. N. R. Rao, Raman evidence for orbiton-mediated multiphonon scattering in multiferroic $TbMnO_3$, J. Phys.: Condens. Matter **22**, 115403 (2010).

[46] I. P. Handayani, N. Mufti, A. A. Nugroho, T. T. M. Palstra, and P. H. M. van Loosdrecht, Raman spectra of multiferroics $TbMnO_3$, Adv. Mater. Res. **1112**, 23 (2015).

[47] S. Mansouri, S. Jandl, A. Mukhin, V. Yu. Ivanov, and Anatoly Balbashov, A comparative Raman study between $PrMnO_3$, $NdMnO_3$, $TbMnO_3$ and $DyMnO_3$, Sci. Rep. **7**, 13796 (2017).

[48] P. Rovillain, M. Cazayous, Y. Gallais, A. Sacuto, M-A. Measson, and H. Sakata, Magnetoelectric excitations in multiferroic $TbMnO_3$ by Raman scattering, Phys. Rev. B **81**, 054428 (2010).

[49] P. Rovillain, J. Liu, M. Cazayous, Y. Gallais, M-A. Measson, H. Sakata, and A. Sacuto, Electromagnon and phonon excitations in multiferroic $TbMnO_3$, Phys. Rev. B **86**, 014437 (2012).

[50] M. N. Iliev, B. Lorenz, A. P. Litvinchuk, Y.-Q. Wang, Y. Y. Sun, and C. W. Chu, Structural, transport, magnetic properties and Raman spectroscopy of orthorhombic $Y_{1-x}Ca_xMnO_3$ ($0 \leqslant x \leqslant 0.5$), J. Phys.: Condens. Matter **17**, 3333 (2005).

[51] M. N. Iliev, V. G. Hadjiev, A. P. Litvinchuk, F. Yen, Y.-Q. Wang, Y. Y. Sun, S. Jandl, J. Laverdière, V. N. Popov, and M. M. Gospodinov, Multiple-order Raman scattering from rare-earth manganites: Oxygen isotope and rare-earth substitution effects, Phys. Rev. B **75**, 064303 (2007).

[52] H. Agarwal, P. Yadav, N. P. Lalla, J. A. Alonso, O. N. Srivastava, and M. A. Shaz, Structural correlation of magnetoelectric coupling in polycrystalline $TbMnO_3$ at low temperature, J. Alloys Compd. **806**, 510 (2019).

[53] J. Menéndez and M. Cardona, Temperature dependence of the first-order Raman scattering by phonons in Si, Ge, and α-Sn: Anharmonic effects, Phys. Rev. B **29**, 2051 (1984).

[54] P. G. Klemens, Anharmonic decay of optical phonons, Phys. Rev. **148**, 845 (1966).

[55] V. G. Hadjiev, Xingjiang Zhou, T. Strohm, M. Cardona, Q. M. Lin, and C. W. Chu, Strong superconductivity-induced phonon self-energy effects in $HgBa_2Ca_3Cu_4O_{10-\delta}$, Phys. Rev. B **58**, 1043 (1998).

[56] M. Rahlenbeck, G. L. Sun, D. L. Sun, C. T. Lin, B. Keimer, and C. Ulrich, Phonon anomalies in pure and underdoped $R_{1-x}K_xFe_2As_2$ (R=Ba, Sr) investigated by Raman light scattering, Phys. Rev. B **80**, 064509 (2009).

[57] S. Jandl, S. Mansouri, A. A. Mukhin, V. Y. Ivanov, A. Balbashov, M. M. Gospodino, V. Nekvasil, and M. Orlita, Study of crystal-field excitations and Raman active phonons in o-$DyMnO_3$, J. Magn. Magn. Mater. **323**, 1104 (2011).

[58] D. Meier, N. Aliouane, D. N. Argyriou, J. A. Mydosh, and T. Lorenz, New features in the phase diagram of $TbMnO_3$, New J. Phys. **9**, 100 (2007).

[59] D. A. Mota, A. Almeida, V. H. Rodrigues, M. M. R. Costa, P. Tavares, P. Bouvier, M. Guennou, J. Kreisel, and J. Agostinho Moreira, Dynamic and structural properties of orthorhombic rare-earth manganites under high pressure, Phys. Rev. B **90**, 054104 (2014).

[60] M. Schmidt, C. Kant, T. Rudolf, F. Mayr, A. A. Mukhin, A. M. Balbashov, J. Deisenhofer, and A. Loidl, Far-infrared optical excitations in multiferroic $TbMnO_3$, Eur. Phys. J. B **71**, 411 (2009).

[61] R. Schleck, R. L. Moreira, H. Sakata, and R. P. S. M. Lobo, Infrared reflectivity of the phonon spectra in multiferroic $TbMnO_3$, Phys. Rev. B **82**, 144309 (2010).

[62] D. J. Lockwood and M. G. Cottam, The spin phonon interaction in FeF_2 and MnF_2 studied by Raman spectroscopy, J. Appl. Phys. **64**, 5876 (1988).